

Efficient Redundancy Reduction for Open-Vocabulary Semantic Segmentation[★]

Lin Chen^{a,b}, Qi Yang^{a,b}, Kun Ding^{a,*}, Zhihao Li^c, Gang Shen^d, Fei Li^d, Qiyuan Cao^{a,b} and Shiming Xiang^{a,b}

^a*State Key Laboratory of Multimodal Artificial Intelligence Systems (MAIS), Institute of Automation, Chinese Academy of Sciences, No. 95 Zhongguancun East Road, Beijing, 100190, China*

^b*School of Artificial Intelligence, University of Chinese Academy of Sciences, No. 19A Yuquan Road, Beijing, 100049, China*

^c*School of Software, Shandong University, No. 1500 Shunhua Road, Jinan, 250101, China*

^d*China Tower Corporation Limited, No. 9 Dongran North Street, Beijing, 100089, China*

ARTICLE INFO

Keywords:

Open-vocabulary
semantic segmentation
vision-language model
redundancy reduction
cost aggregation

ABSTRACT

Open-vocabulary semantic segmentation (OVSS) is an open-world task that aims to assign each pixel within an image to a specific class defined by arbitrary text descriptions. While large-scale vision-language models have shown remarkable open-vocabulary capabilities, their image-level pretraining limits effectiveness on pixel-wise dense prediction tasks like OVSS. Recent cost-based methods narrow this granularity gap by constructing pixel-text cost maps and refining them via cost aggregation mechanisms. Despite achieving promising performance, these approaches suffer from high computational costs and long inference latency. In this paper, we identify two major sources of redundancy in the cost-based OVSS framework: redundant information introduced during cost maps construction and inefficient sequence modeling in cost aggregation. To address these issues, we propose ERR-Seg, an efficient architecture that incorporates Redundancy-Reduced Hierarchical Cost maps (RRHC) and Redundancy-Reduced Cost Aggregation (RRCA). Specifically, RRHC reduces redundant class channels by customizing a compact class vocabulary for each image and integrates hierarchical cost maps to enrich semantic representation. RRCA alleviates computational burden by performing both spatial-level and class-level sequence reduction before aggregation. Overall, ERR-Seg results in a lightweight structure for OVSS, characterized by substantial memory and computational savings without compromising accuracy. Compared to previous state-of-the-art methods on the ADE20K-847 benchmark, ERR-Seg improves performance by 5.6% while achieving a 3.1× speedup. The project page is available at <https://lchen1019.github.io/ERR-Seg>.

1. Introduction

Semantic segmentation is a fundamental task in computer vision that aims to achieve pixel-level semantic understanding. Modern semantic segmentation methods [1–10] rely heavily on large-scale labeled datasets, but can only achieve understanding of limited predefined categories. In contrast, humans can understand scenes in an open-vocabulary manner, enabling the comprehension of arbitrary categories. The pursuit of open-vocabulary semantic segmentation (OVSS) is to replicate this intelligence that can perform unbounded pixel-level semantic understanding. Encouragingly, through natural language supervision, recent large-scale visual-language pre-training models (VLMs) exhibit open-vocabulary comprehension ability. However, existing VLMs receive image-level supervision, which is inadequate for the pixel-level representation required by semantic segmentation. This representation granularity gap

*This research was supported by the National Natural Science Foundation of China under Grant 62306310 and 62433003.

[★]Corresponding author: Kun Ding (kun.ding@ia.ac.cn)

✉ chenlin2024@ia.ac.cn (L. Chen); yangqi2021@ia.ac.cn (Q. Yang); kun.ding@ia.ac.cn (K. Ding); sdulizh@mail.sdu.edu.cn (Z. Li); shengang3@chinatowercom.cn (G. Shen); lifei123457@chinatowercom.cn (F. Li); caoqiyuan2021@ia.ac.cn (Q. Cao); smxiang@nlpr.ia.ac.cn (S. Xiang)

ORCID(s): 0000-0001-6965-1459 (L. Chen); 0000-0001-8373-6096 (Q. Yang); 0000-0002-2256-8815 (K. Ding); 0000-0002-2089-9733 (S. Xiang)

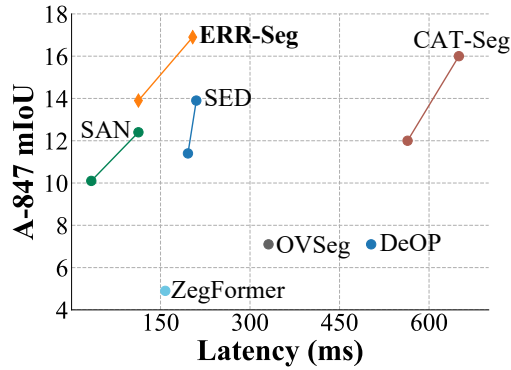


Figure 1: Performance vs. latency on ADE20K-847. Compared with ZegFormer [11], OVSeg [12], DeOP [13], SAN [14], SED [15] and CAT-Seg [16], ERR-Seg achieves a new state-of-the-art with lower latency.

impedes the transfer of open-world knowledge from VLMs to OVSS.

For this issue, recent efforts can be categorized into mask-based and cost-based methods. Mask-based methods [11, 12, 14, 17–23] conceptualize OVSS as the combination of mask generation and open-vocabulary mask classification. These methods necessitate region-level representation, which is much closer to the image-level representation. However, mask-based methods depend on a region proposal network (RPN) to generate masks, which is typically trained

on a specific dataset, lacking the region proposal capability in the open-vocabulary context. To address this issue, several studies [23–26] employ SAM [27] as a universal RPN. Nevertheless, as SAM tends to over-segment an instance into sub-patches, these methods have not made significant progress yet. In contrast, cost-based methods [15, 16] directly generate coarse-grained cost maps by calculating the cosine similarity between dense pixel-level embeddings and text embeddings. These methods effectively bridge the representation granularity gap and eliminate the requirement of RPN. As a result, the methods in this family have shown superior performance compared to mask-based methods.

Although cost-based methods have effectively addressed the challenge of representation granularity, they introduce cost aggregation over pixel-text cost maps, incurring significant computational overhead. Moreover, this overhead grows quadratically with the number of categories, in contrast to the linear growth of mask-based methods. We attribute this issue to two inherent design redundancies in the cost-based methods: (1) **Redundancy in Cost Maps**: It is evident that real-world categories are limitless, while those depicted in an image are always limited, leading to numerous redundant classes. As illustrated in Table 1, images annotated with 847 classes have an average of only 10.2 categories, indicating that there are 98.8% redundant classes. On the one hand, it leads to increased latency due to the redundant class dimension of the cost maps. On the other hand, it poses a challenge for the attention mechanism to model class-level sequences containing numerous redundant classes. (2) **Redundancy in Cost Aggregation**: In closed-set semantic segmentation [2, 5, 8], the fixed class vocabulary enables attention mechanisms to jointly model spatial-class and class-level contextual information with class-informative channels. In contrast, the cost-based OVSS methods require class-agnostic channels due to dynamic class vocabulary, leading to the spatial-level and class-level decoupled attention mechanism in cost aggregation. While effective, it incurs significant computational and memory overhead. Additionally, due to the decoupling, the attention mechanism’s objective is relatively straightforward, potentially containing redundant computations that can be reduced.

To this end, we propose an efficient framework in view of redundancy reduction for OVSS, jointly considering the efficiency and accuracy. To alleviate the redundancy (1), ERR-Seg presents the Redundancy-Reduced Hierarchical Cost maps (RRHC). It first selects the most relevant categories while discarding the others based on the category existence probability implied in the pixel-text cost maps. Additionally, it transforms middle-layer features from CLIP’s image encoder into semantic space to compute hierarchical cost maps in parallel, which are then merged to aggregate more middle-layer semantic details. By reducing the channel dimensions, the attention mechanism can better capture spatial-level long-range dependencies (as depicted in Fig. 2), while also significantly decreasing latency. More comprehensive analyses are provided in Sec. 3.4. To alleviate the

Table 1

Analysis of image category count across five semantic segmentation datasets. It reveals that both PAS-20 (with 20 categories) and A-847 (with 847 categories) contain more than 90% redundant classes.

| | PAS-20 | PC-59 | A-150 | PC-459 | A-847 |
|------------|--------|-------|-------|--------|-------|
| Average | 1.5 | 4.8 | 8.5 | 6.5 | 10.2 |
| Redundancy | 92.5% | 91.9% | 94.3% | 98.6% | 98.8% |

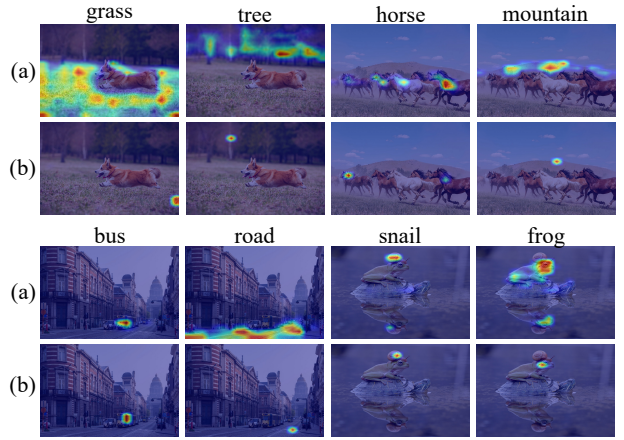


Figure 2: Visual comparison of attention maps during cost aggregation. (a) Using our proposed cost maps (RRHC) with redundancy reduction (48 classes) and (b) using the original full cost maps (847 classes). The results show that the attention mechanism more effectively captures spatial-level long-range dependencies in our proposed RRHC.

redundancy (2), ERR-Seg introduces Redundancy-Reduced Cost Aggregation (RRCA), which incorporates spatial-level and class-level sequence reduction before cost aggregation. This results in a 49.3% reduction in computational workload in cost aggregation without compromising performance. As demonstrated in Fig. 1, ERR-Seg establishes a new state-of-the-art in terms of efficiency and accuracy.

The main contributions can be summarized as follows:

- We introduce an efficient cost-based OVSS framework in view of redundancy reduction, which achieves superior performance on multiple datasets and significantly accelerates the inference process.
- We introduce Redundancy-Reduced Hierarchical Cost maps (RRHC), characterized by dynamic redundant class reduction for each image and hierarchical cost maps extracted from middle-layer features.
- We present the Redundancy-Reduced Cost Aggregation (RRCA) with spatial-level and class-level sequence reduction, substantially accelerating the aggregation process without compromising accuracy.
- We quantitatively and qualitatively investigate the impact of redundancy reduction on modeling spatial-level and class-level contextual information, as well as its effect on computational complexity.

2. Related Work

2.1. Closed-set Semantic Segmentation

From the perspective of modeling semantic segmentation tasks, technical methods can be divided into two categories: (1) Pixel-based methods consider the semantic segmentation task as a dense pixel-by-pixel prediction task. FCN [28] serves as a fundamental pixel-based approach by substituting the fully connected layer in conventional CNNs with a convolutional layer to enable dense category predictions. Subsequently, various pixel-based variants have been developed to incorporate more contextual information, such as dilated convolution [1, 7], feature pyramid [29, 30], pyramid pooling module [30, 31], object contextual representation [8], attention mechanisms [5, 32], pixel contrast [33], prototype view [34] and hierarchical semantic [35, 36]. Additionally, some methods [2, 6, 9, 10, 37–39] introduce transformer-based architectures to semantic segmentation. (2) Mask-based methods [3, 4, 40, 41] treat the segmentation task as a combination of mask generation and mask classification. These methods aim to unify various segmentation tasks (such as instance segmentation, semantic segmentation, and panoptic segmentation) and have demonstrated their effectiveness in the context of closed-set semantic segmentation.

As a fundamental task in computer vision, closed-set semantic segmentation has achieved remarkable success in the past decade, particularly in specific domains such as remote sensing [42, 43], medical segmentation [44] and autonomous driving scenarios [45, 46]. However, this approach relies heavily on large-scale labeled datasets, which require significant human effort to create. Moreover, it is limited to recognizing only a predefined set of categories. This study focuses on OVSS, which can understand arbitrary vocabulary lists, allowing it to address more complex and dynamic scenarios.

2.2. Vision-Language Models

Visual-language models (VLMs) aim to extend open-world comprehension to the visual domain by jointly training visual and language modalities. Early VLMs [47–50] were trained on small-scale datasets through multiple multi-modal tasks. In contrast, CLIP [51] collects large-scale image-text pairs and uses image-text contrastive learning to align the visual and language modality. To further enhance the quality and efficiency of image-text pre-training, ALIGN [52] collected a much larger dataset of image-text pairs without removing noisy data, SigLIP [53] introduces pairwise sigmoid loss to eliminate the requirement of a global view of the pairwise similarities for normalization. Beyond image-text contrast learning, BLIP-2 [54] and LLaVA [55] introduce an additional language model to process aligned images and text in a unified framework for more complex reasoning.

VLMs have been successfully utilized in various multi-modal downstream tasks such as text-to-image generation [56–58], referring segmentation [59, 60], cross-modal retrieval [61, 62] and open-vocabulary understanding [15,

20, 63]. In this study, we better support the application of VLMs to OVSS by enhancing their ability to generate hierarchical semantic maps and leveraging the prior knowledge from VLMs for redundancy reduction.

2.3. Open-Vocabulary Semantic Segmentation

Earlier methods [64–66] for OVSS attempt to establish a joint embedding space connecting image pixels and a predefined vocabulary list. However, these methods struggle with arbitrary class recognition due to their limited vocabulary size. Fortunately, vision-language models (VLM) [51, 52, 67] pre-trained on extensive web data exhibit strong capabilities in open-vocabulary recognition, leading recent research focused on adapting these models for OVSS. Based on the method of introducing semantic information from VLM, current OVSS methods can be categorized into two main groups: mask-based methods and cost-based methods.

For mask-based methods, an intuitive two-stage approach is first proposed. Initially, an additional RPN is adopted to propose region candidates, followed by the application of VLMs for open-vocabulary recognition. ZegFormer [11] and SimBaseline [17] directly adopt this two-stage method, leading to suboptimal performance and significant computational overload. To improve the performance, ODISE [19] utilizes a text-to-image diffusion model as RPN to generate high-quality masks, and OVSeg [12] fine-tunes CLIP on region-text pairs for improved open-vocabulary recognition. To further reduce the computational overload, single-stage methods have been introduced to avoid multiple forward propagations. Among these methods, MaskCLIP [68] and SAN [14] adopt attention bias, while FC-CLIP [20] employs mask pooling. Recent works have introduced various techniques to enhance performance. EBSeg [21] alleviates overfitting to seen training classes via image embedding balancing. MROVSeg [22] tackles the resolution discrepancy by introducing a multi-resolution training framework. SCAN [69] and MAFT+ [70] enhance the fusion of visual and textual features through semantic guidance and a collaborative optimization mechanism, respectively. More recently, OVSNet [71] further avoids overfitting by fusing heterogeneous features and expanding the training space.

For cost-based methods, CAT-Seg [16] aggregates the pixel-text cost maps at both the spatial-level and class-level at one resolution. It also emphasizes the importance of fine-tuning the text encoder of CLIP. In contrast, SED [15] gradually aggregates the cost maps at different resolutions. However, cost-based methods have a drawback compared to mask-based methods: they involve operators with quadratic complexity in relation to the vocabulary size. This means that when the vocabulary is large, it can lead to significant computational and storage overhead. Our proposed ERR-Seg is also cost-based, but we propose to reduce redundancy to alleviate this issue.

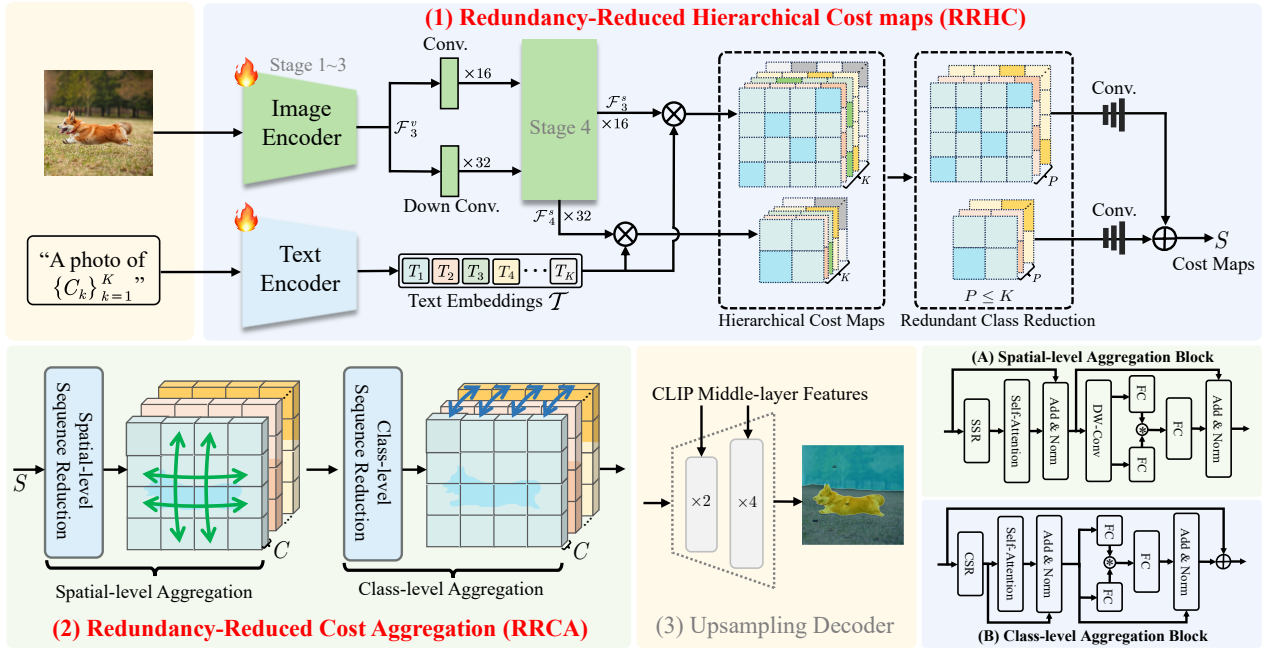


Figure 3: Overall architecture of ERR-Seg. Initially, redundancy-reduced hierarchical cost maps are generated by extracting cost maps from middle-layer features and eliminating class redundancy. Subsequently, the sequence length is reduced before cost aggregation to speed up the computation. Finally, the upsampling decoder restores the high-rank information of cost maps by incorporating image details from the middle-layer features of CLIP’s visual encoder.

3. Methodology

Figure 3 presents an overview of our proposed ERR-Seg. To address the inherent redundancy within the cost-based framework for OVSS, we propose eliminating redundancies in both cost maps and cost aggregation. This section details our redundancy reduction approach for cost maps in Sec. 3.1, followed by the method for reducing redundancy in cost aggregation in Sec. 3.2. Additionally, Sec. 3.3 provides a brief introduction to the upsampling encoder adopted in the cost-based framework. Finally, Sec. 3.4 presents a qualitative and quantitative analysis of the impact of redundancy.

3.1. Redundancy-Reduced Hierarchical Cost Maps

In this section, we present the methodology for constructing our proposed Redundancy-Reduced Hierarchical Cost maps (RRHC). It diverges from previous cost maps in two aspects: (1) Hierarchical Cost Maps: previous methods typically utilize only the last layer output from the CLIP’s image encoder, whereas RRHC also incorporates the features from intermediate layers to build hierarchical cost maps. (2) Redundant Class Reduction: we eliminate redundant classes to derive more concise cost maps customized for each image.

3.1.1. Hierarchical Cost Maps

Typically, cost-based methods introduce semantic information by calculating pixel-text cost maps using only the last layer output, which ignores semantic details from middle-layer features. To address this, we extract semantic

details from the middle-layer features from the CLIP’s image encoders to build hierarchical cost maps.

Initially, I is first encode to derive the middle-layer features $\mathcal{F}_i^v, i \in \{1, 2, 3\}$, and dense image-text aligned embeddings \mathcal{F}_4^s . The relationship between \mathcal{F}_3^v and \mathcal{F}_4^s is modeled as follows:

$$\mathcal{F}_4^s = f_{\text{head}}(g(conv_{s=2}(\mathcal{F}_3^v))), \quad (1)$$

where g represents stage 4 of CLIP’s visual encoder, f_{head} is the linear projection head, and $conv_{s=2}$ denotes convolution with a stride of 2 for downsampling. Additionally, we generate extra image-text aligned embeddings from middle-layer features \mathcal{F}_3^v , as follows:

$$\mathcal{F}_3^s = f_{\text{head}}(g(conv_{s=1}(\mathcal{F}_3^v))), \quad (2)$$

where $conv_{s=1}$ denotes convolution with a stride of 1, using the same initial values as $conv_{s=2}$. $conv_{s=1}$ prevents downsampling, thereby keeping the size of \mathcal{F}_3^s the same as \mathcal{F}_3^v . Notably, we do not construct cost maps from \mathcal{F}_1^v or \mathcal{F}_2^v , as these high-resolution features primarily capture high-frequency details. Therefore, incorporating them during the upsampling stage is sufficient.

Subsequently, by giving $\mathcal{F}_3^v \in \mathbb{R}^{C \times \frac{H}{16} \times \frac{W}{16}}$ and $\mathcal{F}_4^s \in \mathbb{R}^{C \times \frac{H}{32} \times \frac{W}{32}}$, we computes the hierarchical cost maps. Given a vocabulary list $\mathcal{C} = \{C_1, \dots, C_K\}$, a set of sentences $\mathcal{G} = \{G_1, \dots, G_K\}$ is first generated, where G_i consists of C_i and a well-crafted prompt (e.g., “a photo of $\{C_i\}$ in the scene”). \mathcal{G} is then fed into the CLIP’s text encoder to get text embeddings for each class, denoted as $\mathcal{T} = \{T_1, \dots, T_K\}$. The

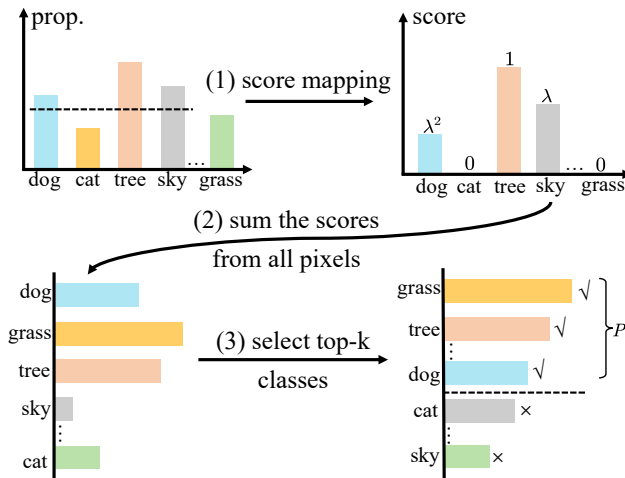


Figure 4: Pipeline of our proposed redundant class reduction mechanism. It involves a training-free scoring function to assign scores to each class, retaining the top- P classes while eliminating other redundant classes.

pixel-text cost maps are derived by calculating the cosine similarity between each pixel and each class:

$$S(i, j, t) = \frac{\mathcal{F}^s(i, j) \cdot \mathcal{T}(t)}{\|\mathcal{F}^s(i, j)\| \|\mathcal{T}(t)\|}, \quad (3)$$

where (i, j) denotes the 2D spatial positions, and t represents the index of text embeddings, $\mathcal{F}^s = \mathcal{F}_3^s$ or \mathcal{F}_4^s . The \mathcal{F}_3^s and \mathcal{F}_4^s are used to derive the pixel-text cost maps $S_3 \in \mathbb{R}^{K \times \frac{H}{16} \times \frac{W}{16}}$ and $S_4 \in \mathbb{R}^{K \times \frac{H}{32} \times \frac{W}{32}}$ individually, combining into our proposed hierarchical cost maps.

3.1.2. Redundant Class Reduction

Based on the observation that the number of classes within an image is limited, we introduce a training-free class selection function Φ , which leverages the prior knowledge in the original cost maps to reduce redundant classes, and determines the top- P classes. Here, $P \leq K$ and P is an empirical value. The impact of P on training and inference will be discussed later.

The pipeline of the function Φ is illustrated in Fig. 4. S represents the probability of each category at each spatial location. Subsequently, for each spatial location, the top k classes are selected based on their probability values and arranged in descending order:

$$N = Top(S, k), \quad (4)$$

where $N \in \mathbb{R}^{k \times H_c \times W_c}$ represents the indices of the top k categories, $H_c \times W_c$ is the size of input cost maps. Then we calculate the scores for each category. The score for t -th category, denoted as $R(t)$, is computed as:

$$R(t) = \sum_{c=1}^k \lambda^{c-1} \left(\sum_{i=1}^{H_c} \sum_{j=1}^{W_c} \mathbb{I}[N(c, i, j) = t] \right), \quad (5)$$

where λ^{c-1} represents the score assigned to the class ranked c . λ is the score coefficient and is expected to meet the condition $0 < \lambda < 1$, as higher-ranked categories should receive higher scores. The notation $\mathbb{I}[\cdot]$ represents a logical expression that yields 1 when the condition is true and 0 otherwise. The cost map used in Φ is S_4 , since it is built from the origin final output of CLIP’s image encoder. After scoring all categories, we obtain $\{R(i)\}_{i=1}^K$, only the top P categories are retained, thus forming redundancy-reduced S_3 and S_4 .

3.1.3. Cost Maps Embedding and Merging

After removing redundant class, we employ a convolution layer with input channel 1 and output channel C to embed the cost maps S_3 and S_4 into the latent space. To aggregate the hierarchical cost maps, we employ a feature pyramid strategy. Specifically, it can be computed as:

$$S \leftarrow \text{conv}(S_3) + \text{up}(\text{conv}(S_4)), \quad (6)$$

where conv denotes a convolution layer, up represents up-sampling interpolation to ensure the same size. Subsequently add them to yield final cost maps $S \in \mathbb{R}^{P \times C \times H_s \times W_s}$, where $H_s = \frac{H}{16}$ and $W_s = \frac{W}{16}$.

3.2. Redundancy-Reduced Cost Aggregation

The cost-based OVSS framework employs spatial-level and class-level decoupled aggregation to enhance contextual information in the coarse-grained cost maps S . Although this aggregation is necessary and effective, it incurs significant computational redundancy due to the attention mechanism modeled across extensive sequence dimensions. Therefore, we introduce Spatial-level Sequence Reduction (SSR) and Class-level Sequence Reduction (CSR) strategies before the aggregation stages. SSR and CSR selectively compress the sequence lengths involved in attention computation, significantly accelerating context fusion while maintaining the segmentation accuracy.

3.2.1. Spatial-level Aggregation

Spatial-level aggregation aims to model the relationships between different spatial locations within the same class. The architecture of the spatial-level aggregation block is presented in Fig. 3 (a). The cost maps S is first reshaped into a spatial-level sequence $S_{\text{spa}} \in \mathbb{R}^{P \times (H_s \times W_s) \times C}$ and then adopt self-attention mechanism, where the sequence length is $H_s \times W_s$. Notably, since the class vocabulary is dynamic in OVSS, the channel dimension C is inherently class-agnostic, thus self-attention operates independently on each class sequence. Although this approach can effectively model intra-class relations, it requires computing self-attention over all $H_s \times W_s$ pixels for every class, leading to substantial computational redundancy.

Recognizing the inherent redundancy in modeling dense interactions across all $H_s \times W_s$ pixels per class, we introduce Spatial-level Sequence Reduction (SSR) to reduce the computational complexity in spatial-level aggregation. Specifically, it reduces the sequence length of S before

reshaping into a spatial-level sequence, as follows:

$$S^r = f_{\text{proj}} \left(\text{conv}_{s=r_1}(S) \right), \quad (7)$$

where $S^r \in \mathbb{R}^{P \times (\frac{H_s}{r_1} \times \frac{W_s}{r_1}) \times C}$, $\text{conv}_{s=r_1}$ is a convolution layer with stride r_1 that performs downsampling on the cost maps while increasing the channel dimension, and f_{proj} represents a linear projection layer that restores the original channel dimension. Subsequently, in the self-attention module, the original sequence S_{spa} serves as query to preserve output dimensions, and the compressed sequence S^r_{spa} functions as key and value.

The output of the self-attention module S_{spa} then passes through a depth-wise convolution layer, followed by a two-layer MLP. Considering SSR compresses the spatial dimension for computational efficiency, it is necessary to enhance the feature representation capacity within the MLP. Therefore, we replace the first linear layer of the MLP with a star operation [72], leveraging its ability to effectively map features into a higher-dimensional space for richer interactions. Specifically, the modified MLP layer is defined as:

$$S_{\text{spa}} \leftarrow f_{\text{out}} \left(\sigma \left(f_{\text{in}}^1(S_{\text{spa}}) \odot f_{\text{in}}^2(S_{\text{spa}}) \right) \right), \quad (8)$$

where, σ denotes the activation function, f_{in}^1 and f_{in}^2 are linear projections mapping from \mathbb{R}^C to $\mathbb{R}^{C'}$, \odot represents element-wise multiplication, f_{out} is the output projection mapping back to \mathbb{R}^C , and C' is the expanded intermediate dimension.

3.2.2. Class-level Aggregation

Class-level aggregation aims to capture dependencies among different classes within the same spatial location. The architecture of our proposed class-level aggregation block is depicted in Fig. 3 (b). It begins by reshaping the cost maps S into a class-level sequence $S_{\text{cls}} \in \mathbb{R}^{(H_s \times W_s) \times P \times C}$, where P is the sequence length for the subsequent self-attention operation. The goal of this self-attention mechanism is to model inter-class relationships, facilitating the identification of the most relevant category for each pixel based on cross-class interactions. However, performing this attention computation over all $H_s \times W_s$ pixels per spatial location is computationally intensive and potentially redundant.

Recognizing that neighboring pixels often share similar features and thus exhibit correlated class dependencies, we introduce the Class-level Sequence Reduction (CSR) strategy. CSR applies an average pooling operation with kernel size $r_2 \times r_2$ and stride r_2 to spatially downsample the cost maps before reshaping. This reduces the spatial dimensions to $\frac{H_s}{r_2} \times \frac{W_s}{r_2}$. Consequently, the reshaped class-level sequence becomes $S_{\text{cls}} \in \mathbb{R}^{(\frac{H_s}{r_2} \times \frac{W_s}{r_2}) \times P \times C}$. Subsequently, the modified MLP in spatial-level aggregation is also employed for improving feature representation capabilities. Finally, the output features are upsampled to the original spatial resolution ($H_s \times W_s$) and added element-wise to the input cost map S . This compression offers dual benefits: (1) it aggregates

information from adjacent pixels into a single representation, providing richer context for category identification at class-level aggregation, and (2) it drastically reduces the sequence length involved in the self-attention computation from $H_s W_s$ to $\frac{H_s W_s}{r_2^2}$, significantly improving computational efficiency.

3.3. Upsampling Decoder

After the cost aggregation, the cost maps S incorporate more contextual information but remain at low resolution, lacking fine-grained edge details. To recover high-resolution semantic maps, we leverage middle-layer visual features \mathcal{F}_i^v extracted from the CLIP image encoder to guide the upsampling of S , following existing practices [16]. Initially, \mathcal{F}_i^v undergoes a convolution layer and is then concatenated with the cost maps at each class. The concatenated features are then passed through a refinement block, comprising two convolution layers. Finally, high-resolution cost maps $S_{\text{hres}} \in \mathbb{R}^{P \times C_h \times \frac{H}{4} \times \frac{W}{4}}$ is obtained, where C_h is the channel dimension of the cost maps, which gradually decreases in the upsampling decoder. Finally, a linear project head project S_{hres} into the size of $P \times (1) \times \frac{H}{4} \times \frac{W}{4}$, to get the final logits.

3.4. Analysis on Redundancy Reduction

A comprehensive analysis of our proposed redundancy reduction is provided in this section, encompassing three aspects: the quantitative analysis of class-level aggregation, the qualitative features of spatial-level aggregation, and the computational complexity.

3.4.1. Impact on class-level aggregation

The original cost maps S comprise the existing and redundant classes. Let $\mathcal{Q}_e = \{S(i)\}_{i=1}^M$ collect the original cost maps corresponding to the existing classes, where M is the number of existing classes in I . The cost maps corresponding to the redundant classes are represented by $\mathcal{Q}_r = \{S(i)\}_{i=M+1}^K$, and those corresponding to the redundant classes after partial reduction are denoted as $\mathcal{Q}_p = \{S(i)\}_{i=M+1}^P$. In the subsequent subsections, we will analyze the impact of \mathcal{Q}_r and \mathcal{Q}_p on class-level and spatial-level aggregation (the primary operations on the cost maps), as well as on latency.

The class-level attention output of the q -th class in \mathcal{Q}_e before reduction is:

$$O^{e,r}(q) = \sum_{k=1}^K \exp \left(\frac{A_{qk}}{\sqrt{C}} \right) S(k) / \sum_{k=1}^K \exp \left(\frac{A_{qk}}{\sqrt{C}} \right), \quad (9)$$

where $q \leq M$, and $A \in \mathbb{R}^{K \times K}$ stands for the class-level attention score matrix before reduction. The contribution of \mathcal{Q}_r to the attention output of the q -th class is formulated as:

$$O^r(q) = \sum_{k=M+1}^K \exp \left(\frac{A_{qk}}{\sqrt{C}} \right) S(k) / \sum_{k=1}^K \exp \left(\frac{A_{qk}}{\sqrt{C}} \right). \quad (10)$$

Similarly, we denote the output of the q -th class after reduction as $O^{e,p}(q)$, and the contribution of \mathcal{Q}_p as $O^p(q)$.

Proposition 1. *The relationship between the contribution ratio of Q_r , denoted as Δ_r , and the contribution ratio of Q_p , denoted as Δ_p , is expressed as:*

$$\Delta_p = \frac{O^p(q)}{O^{e,p}(q)} < \Delta_r = \frac{O^r(q)}{O^{e,r}(q)}. \quad (11)$$

The above inequality suggests that as the number of redundant classes increases, they contribute more to the final output. Thus, existing classes contribute less. As such, we can deduce that reducing redundancy facilitates the class-level aggregation to focus more on existing classes. The proof is detailed in the Appendix.

3.4.2. Impact on spatial-level aggregation

Spatial-level aggregation aims to capture dependencies among different pixels within the same class, it typically assigns high scores when two pixels are close or distant but belong to the same class, indicating similar embeddings. However, after class-level aggregation, each pixel-level embedding integrates contributions from redundant classes. This leads to decreased similarity among pixel-level embeddings of the same class, hindering spatial-level attention from effectively capturing dependencies on distant pixels within the same class. In Fig. 2, we visualize the spatial-level attention maps of different classes, confirming our conclusion that redundancy causes spatial-level attention to focus more on local regions and compromises the ability to capture long-range dependencies.

3.4.3. Impact on computational complexity

The computational efficiency of ERR-Seg is achieved through two redundancy reduction strategies: redundant class dimension reduction from K to P , combined with spatial-level and class-level sequence reduction through downsampling ratios r_1, r_2 . For spatial-level attention, dimensionality compression transforms the spatial sequence from $K \times H_s W_s \times C$ to $P \times \frac{H_s W_s}{r_1^2} \times C$, reducing complexity from $O(KCH_s^2 W_s^2)$ to $O(PCH_s^2 W_s^2 / r_1^2)$. For class-level attention, dimensionality compression transforms complexity from $O(K^2 CH_s W_s)$ to $O(P^2 C \cdot H_s W_s / r_2^2)$. This yields computational savings of $1 - P/(r_1^2 K)$ for spatial-level aggregation and $1 - (P/(r_2 K))^2$ for class-level aggregation.

4. Experiments

4.1. Experimental Setup

4.1.1. Training dataset

Following the existing OVSS methods [15, 16], we train our model on COCO-Stuff [73]. It has 118,287 images for training with 171 different classes.

4.1.2. Evaluation dataset

- **PASCAL-Context** [74] contains 459 classes with 5,104 images for validation. We report the scores of the full classes (PC-459) and the scores of the 59 most frequent classes (PC-59).

Table 2

Label-level similarity between evaluation and training datasets.

| Dataset | 1.00 | ≥ 0.95 | ≥ 0.90 |
|---------|------|-------------|-------------|
| PAS-20 | 0.45 | 0.90 | 1.00 |
| PC-59 | 0.30 | 0.85 | 0.95 |
| A-150 | 0.19 | 0.41 | 0.57 |
| PC-459 | 0.10 | 0.21 | 0.29 |
| A-847 | 0.06 | 0.12 | 0.21 |

- **ADE20K** [75] has 2,000 validation images with 847 classes. Similarly to PASCAL-Context, we report the results of 150 frequent classes (A-150) and full 847 classes (A-847).
- **PASCAL VOC** [76] includes 1,449 images for validation with 20 common object classes. We report the performance of the 20 classes named PAS-20.

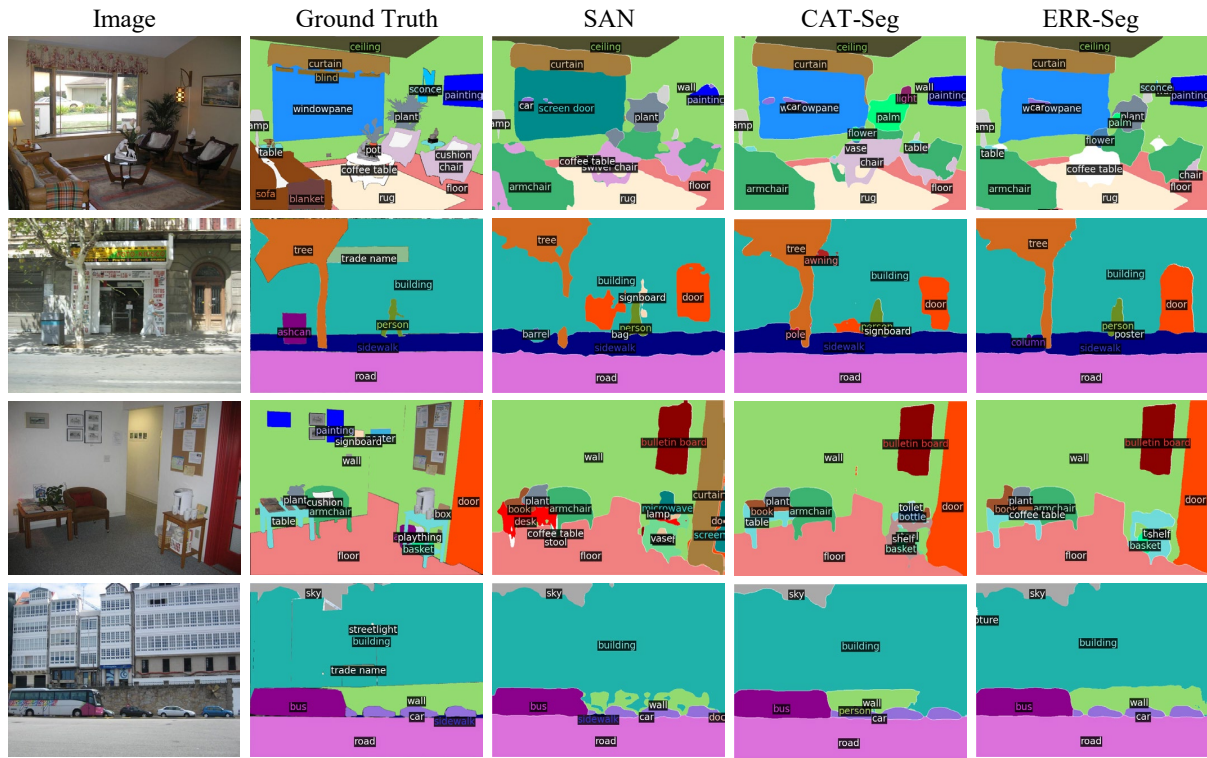
4.1.3. Analysis of the evaluation dataset

Prior studies have typically overlooked the label-level similarity between the validation and training sets, while it is necessary for open vocabulary-related tasks. In this section, we extract text embeddings for each category and then calculate the cosine similarity between the categories in the evaluation and training datasets, resulting in a similarity matrix. Subsequently, we map each category in the evaluation dataset to a category with the highest similarity score in the training dataset. The results are presented in Table 2; we report the proportion of labels in the validation sets with a similarity score equal to 1.00, greater than 0.95, 0.90, and 0.85.

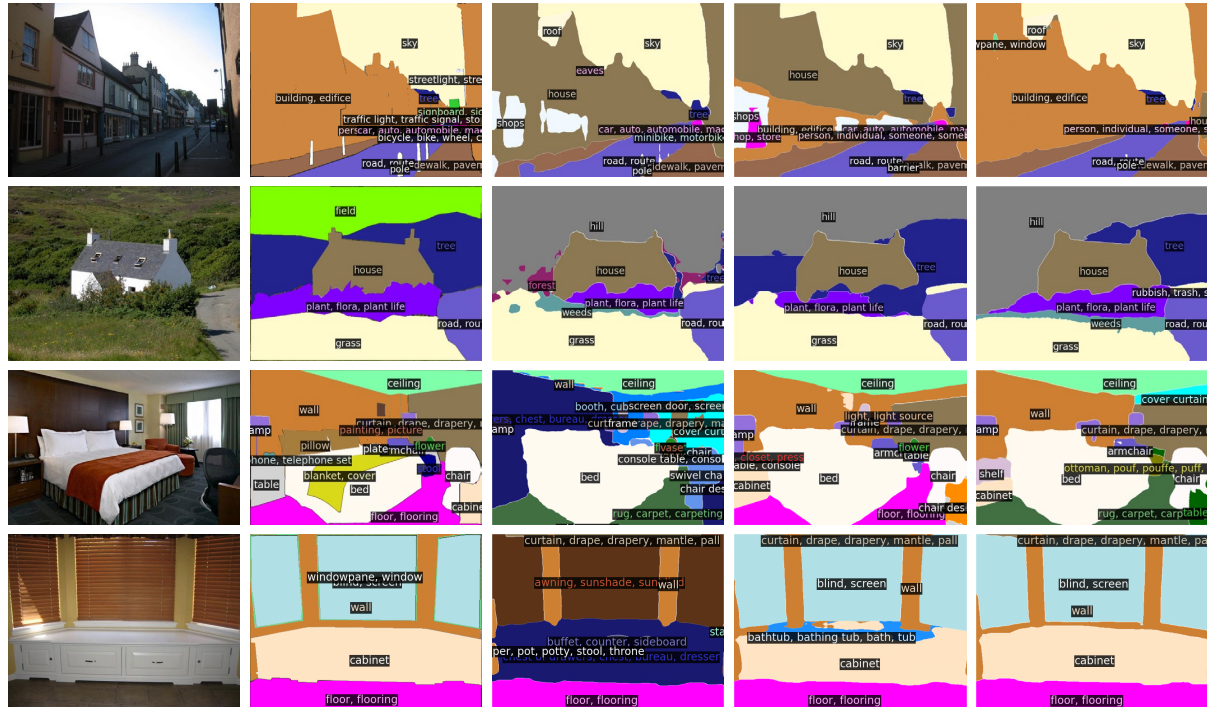
Most categories in PAS-20 and PC-59 display similarity scores exceeding 0.90, indicating that a significant number of categories in these datasets were encountered during the training process. This also implies that overfitting to COCO-Stuff can lead to performance improvement in PAS-20 and PC-59. Hence, PAS-20 and PC-59 measure more in-domain open-vocabulary semantic segmentation capability. In contrast, the ratio is comparatively low for A-150, PC-459, and A-847, suggesting that these three datasets are suitable for measuring out-domain open-vocabulary capability.

4.1.4. Implementation details

We adopt the Convolutional CLIP [77] from Open-CLIP [78], where the visual encoder is ConvNeXt [79] architecture. Our code is implemented on the top of Detectron2 [80]. The AdamW [81] optimizer is employed, with an initial learning rate of 2×10^{-4} and a weight decay of 1×10^{-4} . The learning rate is set to 2×10^{-6} for fine-tuning the CLIP model. We set $\lambda = 0.1, k = 3$ for RRHC and $r_1 = 2, r_2 = 2$ for RRCA. Our model is trained on COCO-Stuff using cross-entropy loss for 80K iterations, with a batch size of 4 and a crop size of 640×640 . 4 NVIDIA RTX 3090 GPUs were used for training.



(a) Qualitative results on ADE20K-150



(b) Qualitative results on ADE20K-847

Figure 5: Visualization of segmentation results on ADE20K-150 and ADE20K-847. The results of previous state-of-the-art methods SAN [15] and CAT-Seg [16] are also included for comparison.

4.2. Main Results

4.2.1. Comparing with state-of-the-art

We compare our proposed ERR-Seg with existing state-of-the-art methods on the five standard evaluation settings,

with the results presented in Table 3. To ensure a fair comparison, all models utilize CLIP as the VLM. We also include whether CLIP's image and text encoders are fine-tuned. When both the image and text encoders are fine-tuned,

Table 3

Comparison with state-of-the-art methods. Img. and Txt. indicate whether the VLM's image and text encoders are fine-tuned, respectively. A.B. signifies whether an additional backbone is employed.

| Method | VLM | Img. | Txt. | A.B. | Training dataset | A-847 | PC-459 | A-150 | PC-59 | PAS-20 |
|------------------|------------|------|------|------|------------------|-------|--------|-------|-------|--------|
| ZegFormer [11] | ViT-B/16 | X | X | ✓ | COCO-Stuff | 5.6 | 10.4 | 18.0 | 45.5 | 89.5 |
| SimBaseline [17] | ViT-B/16 | X | X | ✓ | COCO-Stuff | 7.0 | - | 20.5 | 47.7 | 88.4 |
| OVSeg [12] | ViT-B/16 | ✓ | X | ✓ | COCO-Stuff | 7.1 | 11.0 | 24.8 | 53.3 | 92.6 |
| DeOP [13] | ViT-B/16 | X | X | ✓ | COCO-Stuff-156 | 7.1 | 9.4 | 22.9 | 48.8 | 91.7 |
| SAN [14] | ViT-B/16 | X | X | X | COCO-Stuff | 10.1 | 12.6 | 27.5 | 53.8 | 94.0 |
| EBSeg [21] | ViT-B/16 | X | X | ✓ | COCO-Stuff | 11.1 | 17.3 | 30.0 | 56.7 | 94.6 |
| SED [15] | ConvNeXt-B | ✓ | X | X | COCO-Stuff | 11.4 | 18.6 | 31.6 | 57.3 | 94.4 |
| SCAN [69] | ViT-B/16 | X | X | ✓ | COCO-Stuff | 13.2 | 10.8 | 30.8 | 58.4 | 97.0 |
| MROVSeg [22] | ViT-B/16 | X | X | X | COCO-Stuff | 12.1 | 19.6 | 32.0 | 58.5 | 95.5 |
| CAT-Seg [16] | ViT-B/16 | ✓ | ✓ | X | COCO-Stuff | 12.0 | 19.0 | 31.8 | 57.5 | 94.6 |
| ERR-Seg (ours) | ConvNeXt-B | ✓ | X | X | COCO-Stuff | 11.7 | 18.9 | 32.9 | 56.6 | 94.9 |
| ERR-Seg (ours) | ConvNeXt-B | ✓ | ✓ | X | COCO-Stuff | 13.9 | 20.5 | 35.8 | 56.9 | 95.4 |
| OVSeg [12] | ViT-L/14 | ✓ | X | ✓ | COCO-Stuff | 9.0 | 12.4 | 29.6 | 55.7 | 94.5 |
| ODISE [19] | ViT-L/14 | X | X | ✓ | COCO Panoptic | 11.1 | 14.5 | 29.9 | 57.3 | - |
| SAN [14] | ViT-L/14 | X | X | X | COCO-Stuff | 12.4 | 15.7 | 32.1 | 57.7 | 94.6 |
| FC-CLIP [20] | ConvNeXt-L | X | X | X | COCO Panoptic | 14.8 | 18.2 | 34.1 | 58.4 | 95.4 |
| Unpair-Seg [82] | ConvNext-L | X | X | X | Merged-130K | 14.6 | 19.5 | 32.6 | 52.2 | 93.0 |
| EBSeg [21] | ViT-L/14 | X | X | ✓ | COCO-Stuff | 13.7 | 21.0 | 32.8 | 60.2 | 96.4 |
| SED [15] | ConvNeXt-L | ✓ | X | X | COCO-Stuff | 13.9 | 22.6 | 35.2 | 60.6 | 96.1 |
| MAFT+ [70] | ConvNeXt-L | ✓ | X | X | COCO-Stuff | 15.1 | 21.6 | 36.1 | 59.4 | 96.5 |
| OVSNet [71] | ConvNeXt-L | X | X | X | COCO-Panoptic | 16.2 | 23.5 | 37.1 | 62.0 | 96.9 |
| CAT-Seg [16] | ViT-L/14 | ✓ | ✓ | X | COCO-Stuff | 16.0 | 23.8 | 37.9 | 63.3 | 97.0 |
| ERR-Seg (ours) | ConvNeXt-L | ✓ | X | X | COCO-Stuff | 15.8 | 22.7 | 36.5 | 60.7 | 96.6 |
| ERR-Seg (ours) | ConvNeXt-L | ✓ | ✓ | X | COCO-Stuff | 16.9 | 23.9 | 38.3 | 60.7 | 96.6 |

Table 4

Efficiency comparison. The latency (ms) is computed on a single NVIDIA RTX 3090 GPU.

| Method | A-847 | | | A-150 | | |
|-------------|---------|--------|------|---------|--------|------|
| | Latency | GFLOPs | mIoU | Latency | GFLOPs | mIoU |
| ZegFormer | 158 | 1954 | 4.9 | 154 | 1932 | 16.9 |
| SimBaseline | 331 | 1878 | 7.0 | 329 | 1783 | 20.5 |
| DeOP | 503 | 2791 | 7.1 | 178 | 711 | 22.9 |
| OVSeg | 331 | 1791 | 7.1 | 324 | 1783 | 24.8 |
| SAN | 34 | 120 | 10.1 | 32 | 95 | 27.5 |
| SED | 196 | 571 | 11.4 | 114 | 291 | 31.6 |
| CAT-Seg | 552 | 2154 | 12.0 | 369 | 1516 | 31.8 |
| ERR-Seg | 114 | 348 | 13.9 | 85 | 288 | 35.8 |

ERR-Seg achieves remarkable performance on these five settings, particularly in the base model. Notably, on A-847, PC-459, and A-150, ERR-Seg achieves significant gains, surpassing the previous best results by margins of 5.3%, 7.9%, and 11.9%, respectively. In the large model setting, ERR-Seg continues to outperform prior arts, exceeding the best previous scores on A-847, PC-459, and A-150 by 4.3%, 0.4%, and 1.1%, respectively. When only the text encoder is fine-tuned, ERR-Seg also outperforms SED [15] on all five settings, with an improvement of 13.7%, 0.4%, 5.2%, 0.2% and 0.6% on A-847, PC-459, A-150, PC-59 and PAS-20, respectively.

Table 5

Comparison on seen and unseen classes.

| Method | A-847 | | PC-459 | | A-150 | |
|---------|-------|--------|--------|--------|-------|--------|
| | Seen | Unseen | Seen | Unseen | Seen | Unseen |
| CAT-Seg | 29.2 | 9.6 | 38.3 | 12.5 | 42.1 | 24.4 |
| ERR-Seg | 30.1 | 11.6 | 40.1 | 13.9 | 44.7 | 29.4 |

However, ERR-Seg does not perform as well as CAT-Seg on PC-59, exhibiting a 4.1% lower performance than CAT-Seg in the large model. As discussed in Section 4.1.3, PC-59 primarily assesses in-domain open-vocabulary performance. This indicates that CAT-Seg might fit more of the seen categories during training, thus showcasing superior in-domain performance compared to our model but lagging in out-domain performance. In contrast, with the introduction of redundant class reduction, ERR-Seg customizes the vocabulary list for each image during training, which helps prevent overfitting to the seen categories. A similar trend is observed with SCAN: it outperforms CAT-Seg by 0.9 and 2.4 on PC-59 and PAS-20, respectively, but suffers a significant performance drop of 8.2 on PC-459.

Tab. 5 presents a comparison with CAT-Seg on both seen and unseen classes. Here, unseen classes are defined as those with a label similarity exceeding 0.95 to the COCO-Stuff training set, based on the analysis in Sec. 4.1.3. The results demonstrate that our method not only generalizes effectively from seen to unseen classes, but also achieves

consistent improvements across both settings. Furthermore, our method exhibits more substantial gains on unseen classes relative to CAT-Seg: on the seen classes of A-847, PC-459, and A-150, the relative improvements are 3.1%, 4.7%, and 6.2%, respectively, while on unseen classes, the relative improvements reach 20.8%, 11.2%, and 20.5%.

4.2.2. Efficiency comparison

Table 4 presents the results of the latency comparisons. Although cost-based CAT-Seg shows notable performance enhancement over mask-based SAN, it also results in a considerable increase in latency. In contrast, our proposed ERR-Seg not only further improves the performance of cost-based methods but also reduces their latency significantly. Specifically, the latency is reduced by 79.3% on A-847 and 77.0% on A-150.

4.2.3. Qualitative results

Fig. 5 presents a qualitative comparison among SAN [14], CAT-Seg [16], and our proposed ERR-Seg on the validation sets of ADE20K-150 and ADE20K-847. The results highlight the superiority of our method over previous approaches in mask generation and open-vocabulary recognition. In addition, ERR-Seg can identify targets that were previously overlooked in ADE20K. While the current OVSS model shows remarkable open-vocabulary recognition capability due to the advancements of VLMs, it struggles with segmenting intricate masks. There is still potential for improvement in effectively recognizing small and nested targets.

4.3. Ablation Study and Analysis

4.3.1. Ablation study on RRHC

Table 6 presents the ablation study on RRHC. The results indicate that removing the class redundancy leads to performance increases on some benchmarks, such as +0.4 mIoU on PC-459 and +0.5 mIoU on A-150. This demonstrates that our proposed class redundancy removal strategy can serve not only as a methodology to alleviate computation overload for OVSS but also to improve performance. Moreover, it also demonstrates the effectiveness of our hierarchical cost maps, which leads to +1.2 mIoU improvement on PC-459.

Without RRHC, the gradient for updating stage 4 of CLIP’s visual encoder is derived solely from \mathcal{F}_3^s . However, when using RRHC, the gradient can be sourced from \mathcal{F}_3^s and \mathcal{F}_4^s , as it functions as a parallel branch. Table 6 investigates the impact of different gradient sources on updating stage 4. The results show that relying solely on \mathcal{F}_3^s leads to notably poorer model performance. Furthermore, the combination of gradients from \mathcal{F}_3^s and \mathcal{F}_4^s yields slightly better performance on some benchmarks than relying solely on \mathcal{F}_4^s .

4.3.2. Hyperparameter analysis for RRHC

Fig. 6 illustrates how the score coefficient λ influences class scoring, with optimal performance achieved at $\lambda = 0.1$. A larger λ may blur the distinction between classes with similar rankings, while a smaller λ might overlook certain classes.

Table 6
Ablation study and on RRHC.

| Class redundancy | A-847 | PC-459 | A-150 | PC-59 | PAS-20 |
|-------------------------------------|-------------|-------------|-------------|-------------|-------------|
| w/o remove | 14.0 | 20.1 | 35.3 | 56.8 | 94.9 |
| w/ remove | 13.9 | 20.5 | 35.8 | 56.9 | 95.4 |
| Cost maps | A-847 | PC-459 | A-150 | PC-59 | PAS-20 |
| Single | 13.3 | 19.3 | 35.5 | 56.4 | 95.0 |
| Hierarchical | 13.9 | 20.5 | 35.8 | 56.9 | 95.4 |
| Stage 4 gradient from | A-847 | PC-459 | A-150 | PC-59 | PAS-20 |
| \mathcal{F}_3^s | 7.3 | 13.5 | 20.1 | 45.5 | 90.6 |
| \mathcal{F}_4^s | 14.1 | 20.4 | 35.6 | 57.0 | 94.7 |
| $\mathcal{F}_3^s + \mathcal{F}_4^s$ | 13.9 | 20.5 | 35.8 | 56.9 | 95.4 |

Table 7
Effect of Top k categories.

| Top k categories | A-847 | PC-459 | A-150 | PC-59 | PAS-20 |
|--------------------|-------|--------|-------|-------|--------|
| 1 | 13.8 | 20.5 | 35.8 | 56.9 | 95.4 |
| 3 | 13.9 | 20.5 | 35.8 | 56.9 | 95.4 |
| 5 | 13.8 | 20.5 | 35.8 | 56.8 | 95.4 |

Table 7 presents the effect of the top k categories of a pixel, indicating that the redundant class reduction mechanism is minimally sensitive to k , with slightly superior results observed at $k = 3$. A smaller k , such as 1, risks overlooking existing categories due to potential inaccuracies in cost maps’ prior knowledge. Conversely, a larger k may introduce redundant categories, hindering its ability to identify the most relevant classes.

Fig. 7 explores the effect of the selected class number P during training on the COCO-Stuff dataset, highlighting that setting $P = 32$ yields optimal performance. It also reveals that setting P either too large or too small can hinder the modeling of contextual information. During inference, P is set to the original number of classes of each dataset to ensure a fair comparison.

Table 8 illustrates the influence of the sampled class number P in the redundant class reduction mechanism during the inference phase. It is evident that as P increases gradually, the performance tends to reach a saturation point. The performance is observed to saturate as P increases, consistent with the expectation that a sufficiently large P can encompass all relevant categories. Specifically, we assign the following values to P : 48 for A-847, 48 for PC-459, 32 for A-150, 24 for PC-59, and 16 for PAS-20.

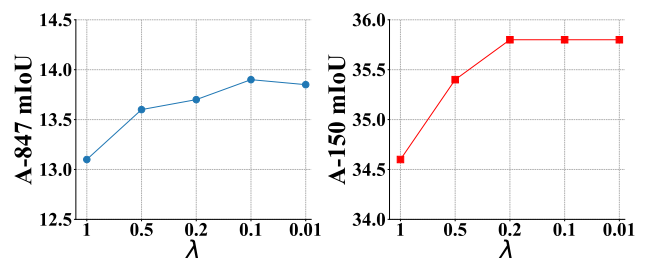


Figure 6: Impact of score coefficient λ .

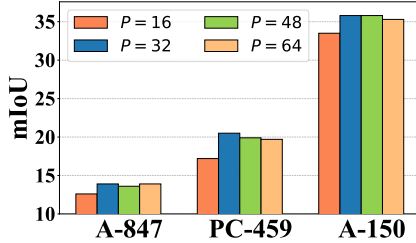


Figure 7: Analysis of selected class number P during training. It indicates that excessively large or small values of P result in performance degradation.

Table 8

The impact of sampled class number P during inference.

| A-847 | | PC-459 | | A-150 | | PC-59 | | PAS-20 | |
|-------|-------|--------|-------|-------|-------|-------|-------|--------|-------|
| P↓ | mIoU↑ | P↓ | mIoU↑ | P↓ | mIoU↑ | P↓ | mIoU↑ | P↓ | mIoU↑ |
| 32 | 13.6 | 16 | 18.8 | 16 | 34.9 | 8 | 54.9 | 4 | 90.2 |
| 48 | 13.9 | 32 | 19.9 | 24 | 35.5 | 16 | 56.9 | 8 | 95.3 |
| 64 | 13.9 | 48 | 20.5 | 32 | 35.8 | 24 | 56.9 | 12 | 95.4 |
| 80 | 13.9 | 64 | 20.5 | 40 | 35.8 | 32 | 57.0 | 16 | 95.4 |

Table 9

Analysis of redundant class removal in RRHC. The “#Classes” columns denote the average number of predicted classes that overlap with the ground truth per image.

| Method | A-847 | | PC-459 | | A-150 | |
|--------------|----------|------|----------|------|----------|------|
| | #Classes | mIoU | #Classes | mIoU | #Classes | mIoU |
| Ground Truth | 10.2 | - | 6.5 | - | 8.5 | - |
| w/o removal | 6.2 | 14.0 | 4.7 | 20.1 | 6.1 | 35.3 |
| w/ removal | 5.7 | 13.9 | 4.4 | 20.5 | 5.9 | 35.8 |

4.3.3. Analysis on RRHC

Table 9 presents the impact of removing redundant classes in RRHC on the final segmentation performance. We report the average number of classes per image in the ground truth, as well as the number of predicted classes overlapping with the ground truth, both before and after redundant class removal. It can be observed that the removal leads to a slight reduction in the number of recognized classes, for instance, on A-150, an average of 0.2 classes per image is no longer detected. Nevertheless, this minor decline is a worthwhile trade-off, as removing redundant classes brings gains in both segmentation accuracy (e.g., 0.4 and 0.5 improvement on PC-459 and A-150, respectively) and inference speed (discussed in Sec. 3.4).

4.3.4. Ablation study on RRCA

RRCA aims to incorporate more contextual information at both the class-level and spatial-level within the cost maps. We first conduct experiments to analyze the spatial-level and class-level aggregation separately. We observed a significant decrease in performance when the spatial-level aggregation and the class-level aggregation are removed, as shown in Table 10. Table 11 presents the effects of the

Table 10

The impact of spatial-level aggregation and class-level aggregation.

| Spatial | Class | A-847 | PC-459 | A-150 | PC-59 | PAS-20 |
|---------|-------|-------|--------|-------|-------|--------|
| ✓ | | 9.3 | 12.8 | 26.1 | 43.6 | 90.8 |
| | ✓ | 13.1 | 19.2 | 34.4 | 56.3 | 94.4 |
| | ✓ | 13.0 | 19.6 | 34.1 | 55.4 | 95.5 |
| ✓ | ✓ | 13.9 | 20.5 | 35.8 | 56.9 | 95.4 |

Table 11

Effect of the Spatial-level Sequence Reduction (SSR) and Class-level Sequence Reduction (CSR).

| SSR | CSR | A-847 | PC-459 | A-150 | PC-59 | GFLOPs | Memory | Latency |
|-----|-----|-------|--------|-------|-------|--------|--------|---------|
| ✓ | | 13.5 | 20.0 | 35.4 | 57.0 | 188.1 | 9.5 | 103 |
| | ✓ | 14.2 | 20.0 | 35.9 | 56.9 | 148.9 | 7.8 | 91 |
| | ✓ | 14.2 | 19.9 | 35.6 | 57.0 | 134.6 | 5.9 | 57 |
| ✓ | ✓ | 13.9 | 20.5 | 35.8 | 56.9 | 95.3 | 4.2 | 49 |

Table 12

Impact of different MLP structures in cost aggregation blocks.

| MLP | A-847 | PC-459 | A-150 | PC-59 | PAS-20 |
|----------|-------------|-------------|-------------|-------------|-------------|
| Vanilla | 14.1 | 20.1 | 35.6 | 56.3 | 94.7 |
| Modified | 13.9 | 20.5 | 35.8 | 56.9 | 95.4 |

sequence reduction strategies, SSR and CSR, including their impact on GFLOPs, memory usage (GiB) and latency (ms). The findings indicate that the use of CSR or SSR alone does not negatively affect performance. Overall, equipping SSR and CSR achieves a reduction of 49.6% GFLOPs, 55.6% memory and 52.4% latency without compromising performance. Additionally, Table 12 compares the effect of different MLP architectures within the cost aggregation blocks. Here, Vanilla refers to the standard MLP consisting of two linear layers and an activation function, while the Modified MLP incorporates the star operation to strengthen its representational capacity. It shows that the performance of ERR-Seg is improved on four datasets by adopting the modified MLP.

4.3.5. Impact of CLIP architecture

Following previous methods [15, 20], our ERR-Seg also adopts the hierarchical CLIP (ConvNeXt) instead of the plain CLIP (ViT). The impact of the CLIP architecture is illustrated in Table 13. To ensure a fair comparison, training and evaluation are conducted using an input size of 384^2 with frozen CLIP. The results show that employing hierarchical CLIP leads to a +2.2 +and +4.1 mIoU improvement on A-847 and A-150, respectively. Furthermore, compared to the ViT-based architecture, it slightly reduces inference latency, with an 8 ms reduction on ADE20K-150. In comparison to plain CLIP, hierarchical CLIP offers the following advantages: (1) it allows the use of middle-layer features to enhance the reconstruction of high-resolution semantic maps, and (2) it permits direct inference on high-resolution

Table 13
Impact of CLIP Architecture.

| CLIP Arch. | Latency | A-847 | PC-459 | A-150 | PC-59 | PAS-20 |
|------------|---------|-------|--------|-------|-------|--------|
| ViT-B/16 | 56 | 7.5 | 13.0 | 22.8 | 49.7 | 91.0 |
| ConvNeXt-B | 47 | 9.7 | 12.5 | 26.9 | 49.4 | 89.9 |

Table 14
The impact of crop size during inference.

| Backbone | Size | A-847 | PC-459 | A-150 | PC-59 | PAS-20 |
|------------|-------------------|-------|--------|-------|-------|--------|
| ConvNeXt-B | 512 ² | 13.7 | 19.8 | 35.1 | 56.7 | 95.3 |
| | 640 ² | 13.9 | 20.5 | 35.8 | 56.9 | 95.4 |
| | 768 ² | 13.5 | 20.1 | 35.7 | 57.1 | 95.1 |
| | 1024 ² | 13.1 | 18.7 | 34.3 | 55.5 | 93.3 |
| ConvNeXt-L | 512 ² | 16.0 | 22.9 | 36.9 | 60.0 | 96.7 |
| | 640 ² | 16.6 | 23.5 | 37.8 | 60.5 | 96.8 |
| | 768 ² | 16.9 | 23.9 | 38.3 | 60.7 | 96.6 |
| | 1024 ² | 16.6 | 23.4 | 38.2 | 59.8 | 96.2 |

images, eliminating the need for the sliding window inference strategy [16] employed in plain CLIP.

4.3.6. Impact of input size

Table 14 presents the results with varying input sizes during the inference phase. The findings highlight a decrease in performance when input sizes are too large or too small. Specifically, for models based on ConvNeXt-B and ConvNeXt-L, the recommended input sizes are 640² and 768², respectively. Our analysis reveals that using ConvNeXt-L as the backbone of CLIP, there is a better alignment between the image and text spaces, enabling the extraction of more refined pixel-text cost maps and thus supporting larger input sizes.

4.3.7. Failure case analysis.

Fig. 5 presents a qualitative analysis of ERR-Seg’s performance. The results indicate that our model can identify small objects, such as the person and cars depicted in Fig. 5 (a). However, the model struggles to segment precise masks for extremely narrow or small objects, such as the table legs and road railings shown in Fig. 5 (a) and (b). Moreover, ERR-Seg demonstrates considerable robustness in parsing complex scenes, such as cluttered indoor environments. Nevertheless, it remains susceptible to semantic misclassification, for instance, confusing a sofa with an armchair in Fig. 5 (a). It is worth noting that addressing these issues remains a key objective in the field of semantic segmentation.

5. Conclusion

In conclusion, we introduced ERR-Seg, an efficient framework for open-vocabulary semantic segmentation. We identified that the redundancy in cost-based methods not only increases computational latency but also hinders the attention mechanism from capturing spatial-level and class-level dependencies. To address this, ERR-Seg

incorporates the Redundancy-Reduced Hierarchical Cost maps (RRHC), which eliminates irrelevant classes using semantic priors from VLMs and incorporates hierarchical cost maps for enriched semantic representation. Furthermore, the Redundancy-Reduced Cost Aggregation (RRCA) significantly reduces computational overhead via sequence compression. Experimental results demonstrate that ERR-Seg establishes a new state-of-the-art in terms of efficiency and accuracy.

Limitations and future work. Our failure case analysis reveals two primary limitations of the proposed OVSS framework: difficulties in generating precise masks for extremely small or narrow objects and inaccuracies in class recognition. We attribute these challenges to the cost aggregation paradigm’s reliance on CLIP for generating dense pixel-text cost maps, which provides insufficient fine-grained visual representations for these challenging scenarios. Future work will enhance the OVSS framework by integrating powerful vision foundation models (e.g., DINO [83], SAM [27]) to improve mask quality and leveraging advanced Multimodal Large Language Models (e.g., Qwen-VL series [84–86]) to provide more robust open-vocabulary recognition capability. Moreover, future work also will focus on designing lightweight learnable class selection module to automatically adapt to diverse vocabularies and image inputs.

A. Appendix

A.1. Proof for Proposition 1

Proof. By utilizing Eq. 9 and Eq. 10, the expression $\Delta_r = O^r(q)/O^{r,r}(q)$ can be simplified as:

$$\Delta_r = \sum_{k=M+1}^K \exp\left(\frac{A_{qk}}{\sqrt{C}}\right) S(k) / \sum_{k=1}^K \exp\left(\frac{A_{qk}}{\sqrt{C}}\right) S(k). \quad (12)$$

Similarly, Δ_p can be simplified as:

$$\Delta_p = \sum_{k=M+1}^P \exp\left(\frac{B_{qk}}{\sqrt{C}}\right) S(k) / \sum_{k=1}^P \exp\left(\frac{B_{qk}}{\sqrt{C}}\right) S(k), \quad (13)$$

where $B \in \mathbb{R}^{P \times P}$ represents the attention scores matrix after redundancy reduction. Let us define:

$$\Delta'_r = \left(\frac{1}{\Delta_r} - 1 \right), \quad (14)$$

$$\Delta'_p = \left(\frac{1}{\Delta_p} - 1 \right). \quad (15)$$

Since $0 < \Delta_r, \Delta_p < 1$, it follows that $\Delta'_r, \Delta'_p > 0$. To compare Δ_r and Δ_p , we first compare Δ'_r and Δ'_p , by analyzing the following formula:

$$\frac{\Delta'_r}{\Delta'_p} = \frac{\sum_{k=1}^M \exp\left(\frac{A_{qk}}{\sqrt{C}}\right) S(k)}{\sum_{k=M+1}^K \exp\left(\frac{A_{qk}}{\sqrt{C}}\right) S(k)} \frac{\sum_{k=M+1}^P \exp\left(\frac{B_{qk}}{\sqrt{C}}\right) S(k)}{\sum_{k=1}^M \exp\left(\frac{B_{qk}}{\sqrt{C}}\right) S(k)}. \quad (16)$$

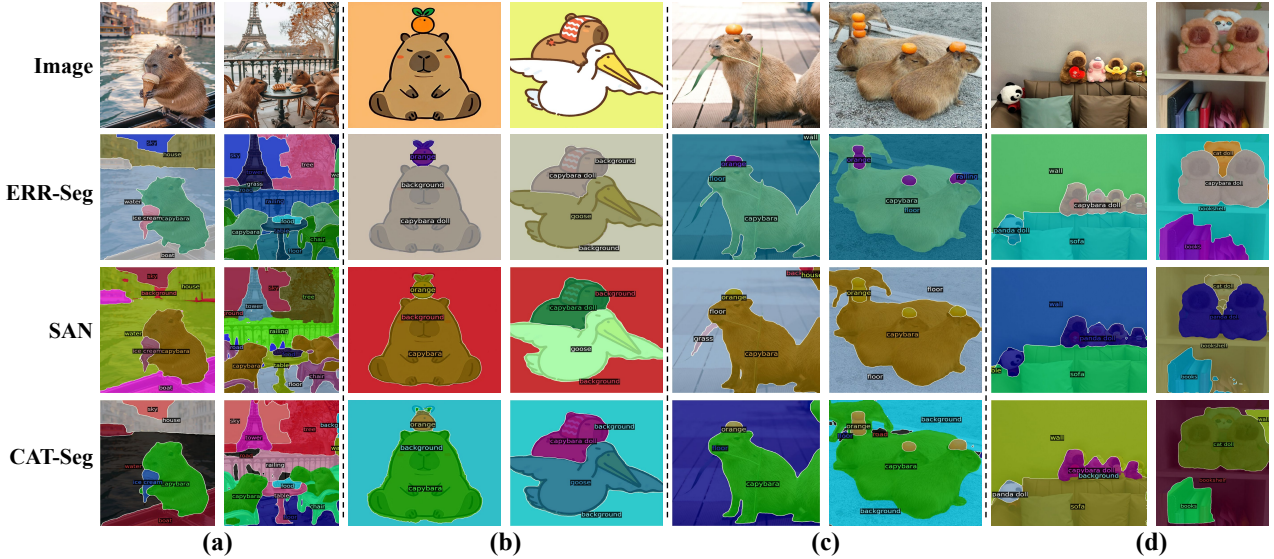


Figure 8: Visualization of segmentation results in various domains. Our proposed ERR-Seg is capable of segmenting capybaras (a rare category in public datasets) from various domains, including (a) synthesized images, (b) cartoon images, (c) natural images, and (d) capybara dolls. Moreover, ERR-Seg achieves more precise masks than SAN [14] and CAT-Seg [16].

Let us define:

$$\alpha = \sum_{k=1}^M \exp\left(\frac{A_{qk}}{\sqrt{C}}\right) S(k) / \sum_{k=1}^M \exp\left(\frac{B_{qk}}{\sqrt{C}}\right) S(k) \quad (17)$$

and

$$\beta = \sum_{k=M+1}^P \exp\left(\frac{B_{qk}}{\sqrt{C}}\right) S(k) / \sum_{k=M+1}^K \exp\left(\frac{A_{qk}}{\sqrt{C}}\right) S(k). \quad (18)$$

Thus, we have

$$\frac{\Delta'_r}{\Delta'_p} = \alpha\beta. \quad (19)$$

Since A and B arise from similarity computations between the same query and key, and redundant categories do not impact the similarity scores of common categories, we have

$$\forall 1 \leq i, j \leq P, A_{ij} = B_{ij}. \quad (20)$$

This implies that $\alpha = 1$ and $\beta < 1$. Hence,

$$\frac{\Delta'_r}{\Delta'_p} = \alpha\beta < 1. \quad (21)$$

It indicates that $\Delta'_r < \Delta'_p$. Thus, we can get $\Delta_p < \Delta_r$. In this way, we finish the proof. \square

A.2. More Qualitative Results

As presented in Fig. 8, ERR-Seg shows its impressive ability to segment and identify capybaras in various domains, highlighting its universal segmentation capability. The selection of capybaras is due to their rarity in public



Vocabulary List = ["capybara standing", "capybara lying", "person", "floor", "stick", "straw", "yellow dog", "white dog", "chair", "wall"]

Figure 9: Visualization of ERR-Seg's attribute understanding. ERR-Seg can correctly distinguish between a yellow dog and a white dog and between a lying capybara and a standing capybara.

datasets. Furthermore, compared with SAN and CAT-Seg, ERR-Seg achieves more precise masks with reduced noise.

Fig. 9 presents two simple examples that illustrate the ability of ERR-Seg to understand attributes such as color and posture. Our model accurately segments dogs of various colors and capybaras in different postures, demonstrating its exceptional open-world understanding capabilities.

References

[1] Liang-Chieh Chen. Rethinking atrous convolution for semantic image segmentation. *arXiv preprint arXiv:1706.05587*, 2017.

[2] Enze Xie, Wenhai Wang, Zhidong Yu, Anima Anandkumar, Jose M Alvarez, and Ping Luo. Segformer: Simple and efficient design for semantic segmentation with transformers. *Advances in Neural Information Processing Systems*, 34:12077–12090, 2021.

[3] Bowen Cheng, Ishan Misra, Alexander G Schwing, Alexander Kirillov, and Rohit Girdhar. Masked-attention mask transformer for universal image segmentation. In *Proceedings of the IEEE/CVF Conference on Computer Vision and Pattern Recognition*, pages 1290–1299, 2022.

[4] Jitesh Jain, Jiachen Li, Mang Tik Chiu, Ali Hassani, Nikita Orlov, and Humphrey Shi. Oneformer: One transformer to rule universal image segmentation. In *Proceedings of the IEEE/CVF Conference on Computer Vision and Pattern Recognition*, pages 2989–2998, 2023.

[5] Jun Fu, Jing Liu, Haijie Tian, Yong Li, Yongjun Bao, Zhiwei Fang, and Hanqing Lu. Dual attention network for scene segmentation. In *Proceedings of the IEEE/CVF Conference on Computer Vision and Pattern Recognition*, pages 3146–3154, 2019.

[6] Robin Strudel, Ricardo Garcia, Ivan Laptev, and Cordelia Schmid. Segmenter: Transformer for semantic segmentation. In *Proceedings of the IEEE/CVF International Conference on Computer Vision*, pages 7262–7272, 2021.

[7] Liang-Chieh Chen, Yukun Zhu, George Papandreou, Florian Schroff, and Hartwig Adam. Encoder-decoder with atrous separable convolution for semantic image segmentation. In *Proceedings of the European Conference on Computer Vision*, pages 801–818, 2018.

[8] Yuhui Yuan, Xilin Chen, and Jingdong Wang. Object-contextual representations for semantic segmentation. In *Proceedings of the European Conference on Computer Vision*, pages 173–190, 2020.

[9] Zhe Chen, Yuchen Duan, Wenhai Wang, Junjun He, Tong Lu, Jifeng Dai, and Yu Qiao. Vision transformer adapter for dense predictions. *arXiv preprint arXiv:2205.08534*, 2022.

[10] Chunlong Xia, Xinliang Wang, Feng Lv, Xin Hao, and Yifeng Shi. Vit-comer: Vision transformer with convolutional multi-scale feature interaction for dense predictions. In *Proceedings of the IEEE/CVF Conference on Computer Vision and Pattern Recognition*, pages 5493–5502, 2024.

[11] Jian Ding, Nan Xue, Gui-Song Xia, and Dengxin Dai. Decoupling zero-shot semantic segmentation. In *Proceedings of the IEEE/CVF Conference on Computer Vision and Pattern Recognition*, pages 11583–11592, 2022.

[12] Feng Liang, Bichen Wu, Xiaoliang Dai, Kunpeng Li, Yinan Zhao, Hang Zhang, Peizhao Zhang, Peter Vajda, and Diana Marculescu. Open-vocabulary semantic segmentation with mask-adapted clip. In *Proceedings of the IEEE/CVF Conference on Computer Vision and Pattern Recognition*, pages 7061–7070, 2023.

[13] Cong Han, Yujie Zhong, Dengjie Li, Kai Han, and Lin Ma. Open-vocabulary semantic segmentation with decoupled one-pass network. In *Proceedings of the IEEE/CVF International Conference on Computer Vision*, pages 1086–1096, 2023.

[14] Mengde Xu, Zheng Zhang, Fangyun Wei, Han Hu, and Xiang Bai. Side adapter network for open-vocabulary semantic segmentation. In *Proceedings of the IEEE/CVF Conference on Computer Vision and Pattern Recognition*, pages 2945–2954, 2023.

[15] Bin Xie, Jiale Cao, Jin Xie, Fahad Shahbaz Khan, and Yanwei Pang. Sed: A simple encoder-decoder for open-vocabulary semantic segmentation. In *Proceedings of the IEEE/CVF Conference on Computer Vision and Pattern Recognition*, pages 3426–3436, 2024.

[16] Seokju Cho, Heeseong Shin, Sunghwan Hong, Anurag Arnab, Paul Hongsuck Seo, and Seungryeong Kim. Cat-seg: Cost aggregation for open-vocabulary semantic segmentation. In *Proceedings of the IEEE/CVF Conference on Computer Vision and Pattern Recognition*, pages 4113–4123, 2024.

[17] Mengde Xu, Zheng Zhang, Fangyun Wei, Yutong Lin, Yue Cao, Han Hu, and Xiang Bai. A simple baseline for open-vocabulary semantic segmentation with pre-trained vision-language model. In *Proceedings of the European Conference on Computer Vision*, pages 736–753, 2022.

[18] Xiaoyi Dong, Jianmin Bao, Yinglin Zheng, Ting Zhang, Dongdong Chen, Hao Yang, Ming Zeng, Weiming Zhang, Lu Yuan, Dong Chen, et al. Maskclip: Masked self-distillation advances contrastive language-image pretraining. In *Proceedings of the IEEE/CVF Conference on Computer Vision and Pattern Recognition*, pages 10995–11005, 2023.

[19] Jiarui Xu, Sifei Liu, Arash Vahdat, Wonmin Byeon, Xiaolong Wang, and Shalini De Mello. Open-vocabulary panoptic segmentation with text-to-image diffusion models. In *Proceedings of the IEEE/CVF Conference on Computer Vision and Pattern Recognition*, pages 2955–2966, 2023.

[20] Qihang Yu, Ju He, Xueqing Deng, Xiaohui Shen, and Liang-Chieh Chen. Convolutions die hard: Open-vocabulary segmentation with single frozen convolutional clip. *Advances in Neural Information Processing Systems*, 36, 2024.

[21] Xiangheng Shan, Dongyue Wu, Guolin Zhu, Yuanjie Shao, Nong Sang, and Changxin Gao. Open-vocabulary semantic segmentation with image embedding balancing. In *Proceedings of the IEEE/CVF Conference on Computer Vision and Pattern Recognition*, pages 28412–28421, 2024.

[22] Yuanbing Zhu, Bingke Zhu, Zhen Chen, Huan Xu, Ming Tang, and Jinqiao Wang. Mrovseg: Breaking the resolution curse of vision-language models in open-vocabulary semantic segmentation. *arXiv preprint arXiv:2408.14776*, 2024.

[23] Pengfei Chen, Lingxi Xie, Xinyue Huo, Xuehui Yu, Xiaopeng Zhang, Yingfei Sun, Zhenjun Han, and Qi Tian. Sam-cp: Marrying sam with composable prompts for versatile segmentation. *arXiv preprint arXiv:2407.16682*, 2024.

[24] Jiaqi Chen, Zeyu Yang, and Li Zhang. Semantic segment anything. <https://github.com/fudan-zvg/Semantic-Segment-Anything>, 2023.

[25] Tianhe Ren, Shilong Liu, Ailing Zeng, Jing Lin, Kunchang Li, He Cao, Jiayu Chen, Xinyu Huang, Yukang Chen, Feng Yan, et al. Grounded sam: Assembling open-world models for diverse visual tasks. *arXiv preprint arXiv:2401.14159*, 2024.

[26] Haoxiang Wang, Pavan Kumar Anasosalu Vasu, Fartash Faghri, Raviteja Vemulapalli, Mehrdad Farajtabar, Sachin Mehta, Mohammad Rastegari, Oncel Tuzel, and Hadi Pouransari. Sam-clip: Merging vision foundation models towards semantic and spatial understanding. In *Proceedings of the IEEE/CVF Conference on Computer Vision and Pattern Recognition*, pages 3635–3647, 2024.

[27] Alexander Kirillov, Eric Mintun, Nikhila Ravi, Hanzi Mao, Chloe Rolland, Laura Gustafson, Tete Xiao, Spencer Whitehead, Alexander C Berg, Wan-Yen Lo, et al. Segment anything. In *Proceedings of the IEEE/CVF International Conference on Computer Vision*, pages 4015–4026, 2023.

[28] Jonathan Long, Evan Shelhamer, and Trevor Darrell. Fully convolutional networks for semantic segmentation. In *Proceedings of the IEEE/CVF Conference on Computer Vision and Pattern Recognition*, pages 3431–3440, 2015.

[29] Alexander Kirillov, Ross Girshick, Kaiming He, and Piotr Dollár. Panoptic feature pyramid networks. In *Proceedings of the IEEE/CVF Conference on Computer Vision and Pattern Recognition*, pages 6399–6408, 2019.

[30] Tete Xiao, Yingcheng Liu, Bolei Zhou, Yuning Jiang, and Jian Sun. Unified perceptual parsing for scene understanding. In *Proceedings of the European Conference on Computer Vision*, pages 418–434, 2018.

[31] Hengshuang Zhao, Jianping Shi, Xiaojuan Qi, Xiaogang Wang, and Jiaya Jia. Pyramid scene parsing network. In *Proceedings of the IEEE/CVF Conference on Computer Vision and Pattern Recognition*, pages 2881–2890, 2017.

[32] Zilong Huang, Xinggang Wang, Lichao Huang, Chang Huang, Yun-chao Wei, and Wenyu Liu. Ccnet: Criss-cross attention for semantic segmentation. In *Proceedings of the IEEE/CVF International Conference on Computer Vision*, pages 603–612, 2019.

[33] Wenguan Wang, Tianfei Zhou, Fisher Yu, Jifeng Dai, Ender Konukoglu, and Luc Van Gool. Exploring cross-image pixel contrast

for semantic segmentation. In *Proceedings of the IEEE/CVF international conference on computer vision*, pages 7303–7313, 2021.

[34] Tianfei Zhou, Wenguan Wang, Ender Konukoglu, and Luc Van Gool. Rethinking semantic segmentation: A prototype view. In *Proceedings of the IEEE/CVF conference on computer vision and pattern recognition*, pages 2582–2593, 2022.

[35] Liulei Li, Tianfei Zhou, Wenguan Wang, Jianwu Li, and Yi Yang. Deep hierarchical semantic segmentation. In *Proceedings of the IEEE/CVF conference on computer vision and pattern recognition*, pages 1246–1257, 2022.

[36] Liulei Li, Wenguan Wang, and Yi Yang. Logicseg: Parsing visual semantics with neural logic learning and reasoning. In *Proceedings of the IEEE/CVF international conference on computer vision*, pages 4122–4133, 2023.

[37] Sixiao Zheng, Jiachen Lu, Hengshuang Zhao, Xiatian Zhu, Zekun Luo, Yabiao Wang, Yanwei Fu, Jianfeng Feng, Tao Xiang, Philip HS Torr, et al. Rethinking semantic segmentation from a sequence-to-sequence perspective with transformers. In *Proceedings of the IEEE/CVF Conference on Computer Vision and Pattern Recognition*, pages 6881–6890, 2021.

[38] Jiaqi Gu, Hyoukjun Kwon, Dilin Wang, Wei Ye, Meng Li, Yu-Hsin Chen, Liangzhen Lai, Vikas Chandra, and David Z Pan. Multi-scale high-resolution vision transformer for semantic segmentation. In *Proceedings of the IEEE/CVF conference on computer vision and pattern recognition*, pages 12094–12103, 2022.

[39] James Liang, Tianfei Zhou, Dongfang Liu, and Wenguan Wang. Clustseg: Clustering for universal segmentation. *arXiv preprint arXiv:2305.02187*, 2023.

[40] Bowen Cheng, Alex Schwing, and Alexander Kirillov. Per-pixel classification is not all you need for semantic segmentation. *Advances in neural information processing systems*, 34:17864–17875, 2021.

[41] Wenwei Zhang, Jiangmiao Pang, Kai Chen, and Chen Change Loy. K-net: Towards unified image segmentation. *Advances in Neural Information Processing Systems*, 34:10326–10338, 2021.

[42] Xianping Ma, Qianqian Wu, Xingyu Zhao, Xiaokang Zhang, Man-On Pun, and Bo Huang. Sam-assisted remote sensing imagery semantic segmentation with object and boundary constraints. *IEEE Transactions on Geoscience and Remote Sensing*, 2024.

[43] Jie Geng, Shuai Song, and Wen Jiang. Dual-path feature aware network for remote sensing image semantic segmentation. *IEEE Transactions on Circuits and Systems for Video Technology*, 2023.

[44] Tao Zhou, Yi Zhou, Guangyu Li, Geng Chen, and Jianbing Shen. Uncertainty-aware hierarchical aggregation network for medical image segmentation. *IEEE Transactions on Circuits and Systems for Video Technology*, 2024.

[45] Zhiyuan Wu, Yi Feng, Chuang-Wei Liu, Fisher Yu, Qijun Chen, and Rui Fan. S³ m-net: Joint learning of semantic segmentation and stereo matching for autonomous driving. *IEEE Transactions on Intelligent Vehicles*, 2024.

[46] Xuepeng Chang, Huihui Pan, Weichao Sun, and Huijun Gao. A multi-phase camera-lidar fusion network for 3d semantic segmentation with weak supervision. *IEEE Transactions on Circuits and Systems for Video Technology*, 33(8):3737–3746, 2023.

[47] Yen-Chun Chen, Linjie Li, Licheng Yu, Ahmed El Kholy, Faisal Ahmed, Zhe Gan, Yu Cheng, and Jingjing Liu. Uniter: Learning universal image-text representations. 2019.

[48] Weijie Su, Xizhou Zhu, Yue Cao, Bin Li, Lewei Lu, Furu Wei, and Jifeng Dai. Vl-bert: Pre-training of generic visual-linguistic representations. *arXiv preprint arXiv:1908.08530*, 2019.

[49] Jiasen Lu, Dhruv Batra, Devi Parikh, and Stefan Lee. Vilbert: Pretraining task-agnostic visiolinguistic representations for vision-and-language tasks. *Advances in Neural Information Processing Systems*, 32, 2019.

[50] Xiuju Li, Xi Yin, Chunyuan Li, Pengchuan Zhang, Xiaowei Hu, Lei Zhang, Lijuan Wang, Houdong Hu, Li Dong, Furu Wei, et al. Oscar: Object-semantics aligned pre-training for vision-language tasks. In *Computer Vision–ECCV 2020: 16th European Conference, Glasgow, UK, August 23–28, 2020, Proceedings, Part XXXI 16*, pages 121–137. Springer, 2020.

[51] Alec Radford, Jong Wook Kim, Chris Hallacy, Aditya Ramesh, Gabriel Goh, Sandhini Agarwal, Girish Sastry, Amanda Askell, Pamela Mishkin, Jack Clark, et al. Learning transferable visual models from natural language supervision. In *International Conference on Machine Learning*, pages 8748–8763, 2021.

[52] Chao Jia, Yinfei Yang, Ye Xia, Yi-Ting Chen, Zarana Parekh, Hieu Pham, Quoc Le, Yun-Hsuan Sung, Zhen Li, and Tom Duerig. Scaling up visual and vision-language representation learning with noisy text supervision. In *International Conference on Machine Learning*, pages 4904–4916, 2021.

[53] Xiaohua Zhai, Basil Mustafa, Alexander Kolesnikov, and Lucas Beyer. Sigmoid loss for language image pre-training. In *Proceedings of the IEEE/CVF International Conference on Computer Vision*, pages 11975–11986, 2023.

[54] Junnan Li, Dongxu Li, Silvio Savarese, and Steven Hoi. Blip-2: Bootstrapping language-image pre-training with frozen image encoders and large language models. In *International conference on machine learning*, pages 19730–19742. PMLR, 2023.

[55] Haotian Liu, Chunyuan Li, Qingyang Wu, and Yong Jae Lee. Visual instruction tuning. *Advances in Neural Information Processing Systems*, 36, 2024.

[56] Aditya Ramesh, Prafulla Dhariwal, Alex Nichol, Casey Chu, and Mark Chen. Hierarchical text-conditional image generation with clip latents. *arXiv preprint arXiv:2204.06125*, 1(2):3, 2022.

[57] Lvmian Zhang, Anyi Rao, and Maneesh Agrawala. Adding conditional control to text-to-image diffusion models, 2023.

[58] Zhicai Wang, Ouxiang Li, Tan Wang, Longhui Wei, Yanbin Hao, Xiang Wang, and Qi Tian. Prior preserved text-to-image personalization without image regularization. *IEEE Transactions on Circuits and Systems for Video Technology*, 2024.

[59] Zhaoqing Wang, Yu Lu, Qiang Li, Xunqiang Tao, Yandong Guo, Mingming Gong, and Tongliang Liu. Cris: Clip-driven referring image segmentation. In *Proceedings of the IEEE/CVF conference on computer vision and pattern recognition*, pages 11686–11695, 2022.

[60] Chao Shang, Hongliang Li, Heqian Qiu, Qingbo Wu, Fanman Meng, Taijin Zhao, and King Ng Ngan. Cross-modal recurrent semantic comprehension for referring image segmentation. *IEEE Transactions on Circuits and Systems for Video Technology*, 33(7):3229–3242, 2022.

[61] Qingrong Cheng, Zhenshan Tan, Keyu Wen, Cheng Chen, and Xiaodong Gu. Semantic pre-alignment and ranking learning with unified framework for cross-modal retrieval. *IEEE Transactions on Circuits and Systems for Video Technology*, 2022.

[62] Jiaxing Li, Wai Keung Wong, Lin Jiang, Xiaozhao Fang, Shengli Xie, and Yong Xu. Ckdh: Clip-based knowledge distillation hashing for cross-modal retrieval. *IEEE Transactions on Circuits and Systems for Video Technology*, 2024.

[63] Shilong Liu, Zhaoyang Zeng, Tianhe Ren, Feng Li, Hao Zhang, Jie Yang, Qing Jiang, Chunyuan Li, Jianwei Yang, Hang Su, et al. Grounding dino: Marrying dino with grounded pre-training for open-set object detection. In *European Conference on Computer Vision*, pages 38–55. Springer, 2024.

[64] Maxime Bucher, Tuan-Hung Vu, Matthieu Cord, and Patrick Pérez. Zero-shot semantic segmentation. *Advances in Neural Information Processing Systems*, 32, 2019.

[65] Yongqin Xian, Subhabrata Choudhury, Yang He, Bernt Schiele, and Zeynep Akata. Semantic projection network for zero-and few-label semantic segmentation. In *Proceedings of the IEEE/CVF Conference on Computer Vision and Pattern Recognition*, pages 8256–8265, 2019.

[66] Hang Zhao, Xavier Puig, Bolei Zhou, Sanja Fidler, and Antonio Torralba. Open vocabulary scene parsing. In *Proceedings of the IEEE International Conference on Computer Vision*, pages 2002–2010, 2017.

[67] Junnan Li, Dongxu Li, Caiming Xiong, and Steven Hoi. Blip: Bootstrapping language-image pre-training for unified vision-language understanding and generation. In *International Conference on Machine*

Learning, pages 12888–12900, 2022.

[68] Zheng Ding, Jieke Wang, and Zhuowen Tu. Open-vocabulary universal image segmentation with maskclip. *arXiv preprint arXiv:2208.08984*, 2022.

[69] Yong Liu, Sule Bai, Guanbin Li, Yitong Wang, and Yansong Tang. Open-vocabulary segmentation with semantic-assisted calibration. In *Proceedings of the IEEE/CVF Conference on Computer Vision and Pattern Recognition*, pages 3491–3500, 2024.

[70] Siyu Jiao, Hongguang Zhu, Jiannan Huang, Yao Zhao, Yunchao Wei, and Humphrey Shi. Collaborative vision-text representation optimizing for open-vocabulary segmentation. In *European Conference on Computer Vision*, pages 399–416. Springer, 2024.

[71] Yong Liu, SongLi Wu, Sule Bai, Jiahao Wang, Yitong Wang, and Yansong Tang. Stepping out of similar semantic space for open-vocabulary segmentation. *arXiv preprint arXiv:2506.16058*, 2025.

[72] Xu Ma, Xiyang Dai, Yue Bai, Yizhou Wang, and Yun Fu. Rewrite the stars. In *Proceedings of the IEEE/CVF Conference on Computer Vision and Pattern Recognition*, pages 5694–5703, 2024.

[73] Holger Caesar, Jasper Uijlings, and Vittorio Ferrari. Coco-stuff: Thing and stuff classes in context. In *Proceedings of the IEEE/CVF Conference on Computer Vision and Pattern Recognition*, pages 1209–1218, 2018.

[74] Roozbeh Mottaghi, Xianjie Chen, Xiaobai Liu, Nam-Gyu Cho, Seong-Whan Lee, Sanja Fidler, Raquel Urtasun, and Alan Yuille. The role of context for object detection and semantic segmentation in the wild. In *Proceedings of the IEEE/CVF Conference on Computer Vision and Pattern Recognition*, pages 891–898, 2014.

[75] Bolei Zhou, Hang Zhao, Xavier Puig, Tete Xiao, Sanja Fidler, Adela Barriuso, and Antonio Torralba. Semantic understanding of scenes through the ade20k dataset. *International Journal of Computer Vision*, 127:302–321, 2019.

[76] Mark Everingham, Luc Van Gool, Christopher KI Williams, John Winn, and Andrew Zisserman. The pascal visual object classes (voc) challenge. *International Journal of Computer Vision*, 88:303–338, 2010.

[77] Mehdi Cherti, Romain Beaumont, Ross Wightman, Mitchell Wortsman, Gabriel Ilharco, Cade Gordon, Christoph Schuhmann, Ludwig Schmidt, and Jenia Jitsev. Reproducible scaling laws for contrastive language-image learning. In *Proceedings of the IEEE/CVF Conference on Computer Vision and Pattern Recognition*, pages 2818–2829, 2023.

[78] Gabriel Ilharco, Mitchell Wortsman, Ross Wightman, Cade Gordon, Nicholas Carlini, Rohan Taori, Achal Dave, Vaishaal Shankar, Hongseok Namkoong, John Miller, Hannaneh Hajishirzi, Ali Farhadi, and Ludwig Schmidt. Openclip, July 2021. If you use this software, please cite it as below.

[79] Zhuang Liu, Hanzi Mao, Chao-Yuan Wu, Christoph Feichtenhofer, Trevor Darrell, and Saining Xie. A convnet for the 2020s. In *Proceedings of the IEEE/CVF Conference on Computer Vision and Pattern Recognition*, pages 11976–11986, 2022.

[80] Yuxin Wu, Alexander Kirillov, Francisco Massa, Wan-Yen Lo, and Ross Girshick. Detectron2. <https://github.com/facebookresearch/detectron2>, 2019.

[81] I Loshchilov. Decoupled weight decay regularization. *arXiv preprint arXiv:1711.05101*, 2017.

[82] Zhaoqing Wang, Xiaobo Xia, Ziye Chen, Xiao He, Yandong Guo, Mingming Gong, and Tongliang Liu. Open-vocabulary segmentation with unpaired mask-text supervision. *arXiv preprint arXiv:2402.08960*, 2024.

[83] Oriane Siméoni, Huy V Vo, Maximilian Seitzer, Federico Baldassarre, Maxime Oquab, Cijo Jose, Vasil Khalidov, Marc Szafraniec, Seungeun Yi, Michaël Ramamonjisoa, et al. Dinov3. *arXiv preprint arXiv:2508.10104*, 2025.

[84] Jinze Bai, Shuai Bai, Shusheng Yang, Shijie Wang, Sinan Tan, Peng Wang, Junyang Lin, Chang Zhou, and Jingren Zhou. Qwen-vl: A versatile vision-language model for understanding, localization, text reading, and beyond. *arXiv preprint arXiv:2308.12966*, 2023.

[85] Peng Wang, Shuai Bai, Sinan Tan, Shijie Wang, Zhihao Fan, Jinze Bai, Kegin Chen, Xuejing Liu, Jialin Wang, Wenbin Ge, Yang Fan, Kai Dang, Mengfei Du, Xuancheng Ren, Rui Men, Dayiheng Liu, Chang Zhou, Jingren Zhou, and Junyang Lin. Qwen2-vl: Enhancing vision-language model’s perception of the world at any resolution. *arXiv preprint arXiv:2409.12191*, 2024.

[86] Shuai Bai, Kegin Chen, Xuejing Liu, Jialin Wang, Wenbin Ge, Sibo Song, Kai Dang, Peng Wang, Shijie Wang, Jun Tang, Humen Zhong, Yuanzhi Zhu, Mingkun Yang, Zhaohai Li, Jianqiang Wan, Pengfei Wang, Wei Ding, Zheren Fu, Yiheng Xu, Jiabo Ye, Xi Zhang, Tianbao Xie, Zesen Cheng, Hang Zhang, Zhibo Yang, Haiyang Xu, and Junyang Lin. Qwen2.5-vl technical report. *arXiv preprint arXiv:2502.13923*, 2025.